Organic Geochemistry 112 (2017) 105–118

Contents lists available at ScienceDirect

Organic Geochemistry

journal homepage: www.elsevier.com/locate/orggeochem

Jump in the structure of Type I kerogen revealed from pyrolysis and ^{13}C DP MAS NMR

Yuan Gao [a,b], Yan-Rong Zou [a,*], Tian Liang [a,b], Ping'an Peng [a,b,*]

[a] State Key Laboratory of Organic Geochemistry, Guangzhou Institute of Geochemistry, Chinese Academy of Sciences, Guangzhou 510640, China
[b] University of Chinese Academy of Sciences, Beijing 100049, China

ARTICLE INFO

Article history:
Received 10 February 2017
Received in revised form 22 June 2017
Accepted 7 July 2017
Available online 18 July 2017

Keywords:
^{13}C NMR
Aromaticity
Kerogen
Chemical structure
Thermal maturity

ABSTRACT

Artificial maturation of Maoming oil shale kerogen (Type I) was performed at a heating rate of 5 °C/h in a closed Au tube system. Yields of pyrolysis products (C_{1-5}, C_{6-14}, C_{14+} and insoluble residue) were quantified. The insoluble kerogen residue was analyzed using Rock-Eval, elemental analysis and quantitative ^{13}C direct polarization/magic angle spinning (DP MAS) nuclear magnetic resonance (NMR) spectroscopy. Peak oil generation was achieved at Easy $\%R_o$ 0.95. A "three-stage" relationship existed between aromaticity and Easy $\%R_o$ because of the relatively pronounced cleavage of aliphatic carbons and the formation of new aromatic structures in the kerogen residue. Five models of kerogen representing five stages in the oil window were drawn to provide a visualized kerogen structure modification with evolution. A novel jump in the structure of the kerogen residue was observed at ca. Easy $\%R_o$ 0.80–0.90, corresponding to the peak oil window. Our results suggest that aromatic carbon, replacing aliphatic carbon and becoming the dominant carbon in the residue, was the cause of the dramatic changes in the Easy $\%R_o$ interval of 0.80–0.90. Both aliphatic and aromatic structures contributed to hydrocarbon generation before peak oil generation. CH_2 groups contributed most to the hydrocarbon generation potential. Me groups contributed little to hydrocarbon generation within the oil window.

1. Introduction

Kerogen is a major component of sedimentary organic matter (OM), is insoluble in common solvents and can be converted to gas and oil under geothermal degradation (Durand-Souron, 1980). It can be classified as Type I, II and III depending on its paleo-environmental origin and composition (Tissot and Welte, 1984). Type I kerogen is composed predominantly of lacustrine algal material and has a high atomic H/C ratio. It occurs mainly in lacustrine environments and has the greatest oil potential (Vandenbroucke and Largeau, 2007). Several sets of Type I kerogen-containing oil shales occur in lacustrine basins in China, e.g. the Maoming oil shale deposited in the Maoming Basin and the Yanchang shale deposited in the Ordos Basin (Qian and Yin, 2008). Therefore, knowledge of Type I kerogen structure and properties is important for petroleum exploration in China. The amount and components of the oil and gas formed during kerogen evolution are dependent on kerogen composition. Meanwhile, generation of hydrocarbons results in measurable structural changes in the solid residue. A better knowledge of kerogen structure and the modifications produced during its evolution contribute to understanding the mechanisms of oil production in nature (Rouxhet and Robin, 1978).

Various solid state nuclear magnetic resonance (NMR) studies have been aimed at characterizing the structural changes in kerogen during maturation. Enhancement of kerogen aromaticity with increasing maturity has been documented by a number of authors (Dennis et al., 1982; Witte et al., 1988; Qin et al., 1991; Patience et al., 1992; Wei et al., 2005; Mao et al., 2010; Fletcher et al., 2014; Clough et al., 2015). Several authors found a linear relationship between NMR-derived aromaticity (f_a) and vitrinite reflectance (R_o) for Type II kerogen (Werner-Zwanziger et al., 2005; Mao et al., 2010). According to Carr and Williamson (1989), a plot of f_a and R_o for coal shows a non-linear relationship with a steep slope when R_o is <0.7%. However, few quantitative ^{13}C direct polarization/magic angle spinning (DP MAS) NMR spectra of Type I kerogen as a measure of maturation have been presented (Fletcher et al., 2014). Previous studies found that, during petroleum generation, the aliphatic carbon content decreased and the aromatic carbon content increased significantly in a narrow maturation

* Corresponding authors at: State Key Laboratory of Organic Geochemistry, Guangzhou Institute of Geochemistry, Chinese Academy of Sciences, Guangzhou 510640, China (Y.-R. Zou, P. Peng).
E-mail addresses: zouyr@gig.ac.cn (Y.-R. Zou), pinganp@gig.c.cn (P. Peng).

http://dx.doi.org/10.1016/j.orggeochem.2017.07.004
0146-6380/

window. However, no studies have clearly noted the specific R_o interval and the cause (Mao et al., 2010).

Over recent decades, the structure of different kerogens has been studied using various physical or chemical methods (Yen, 1976; Behar and Vandenbroucke, 1987; Siskin et al., 1995; Li et al., 2014; Tong et al., 2016). Given its complex macromolecular structure, it is impossible to represent a true kerogen structure, and any detailed model can only represent an average structure (Vandenbroucke, 2003). By accounting for a great amount of information from various analyses, a kerogen model can provide a synthetic view of the main similarities and can be used for comparison of OM types and for the evaluation of kerogen evolution. Vandenbroucke (1980) described the main differences in the structural components of kerogens according to type at the onset of the oil window.

Here, structural models of the immature kerogen of the Maoming oil shale and four residues with different maturity obtained from pyrolysis were constructed on the basis of elemental analysis and structural parameters derived from ^{13}C direct polarization/magic angle spinning NMR ^{13}C DP MAS NMR. A series of structures, representing the different stages of thermal evolution, can provide a visualized image of the structure modification during maturation. As stated by Behar et al. (1987) and Vandenbroucke (2003), these models have only a statistical significance, taking into account the entire data. The real structure of kerogen is much more complex than shown in the models.

This study presents data on the composition and yield of pyrolysis products, using a combination of quantitative ^{13}C DP MAS NMR data and elemental and Rock-Eval analysis, to evaluate the structural changes in a lacustrine Type I kerogen isolated from the Maoming oil shale. A narrow sampling space was planned within a maturity range of 0.60–1.60 $\%R_o$, which includes the "oil window" and part of the "wet gas" stage. On the basis of quantitative ^{13}C DP MAS NMR spectra, the fraction of aromatic and aliphatic carbons can be obtained to identify the relationship between the structural parameters and maturity (R_o). Together with the hydrocarbon products generated, we try to explain the changes in and causes of the Type I kerogen structure jump to better understand its thermal evolution and the mechanism of the transformation from kerogen to petroleum during hydrocarbon generation.

2. Samples and method

The typical Type I kerogen sample (MM9) represents the Oligocene Youganwo Formation oil shale and was obtained from the Jintang outcrop section in the Maoming Basin, southern China. It has total organic carbon (TOC) content 17.48%, hydrogen index (HI) 708.92 mg hydrocarbon (HC)/g TOC, T_{max} 434 °C and an R_o 0.43%. These parameters confirm that the sample was immature and contained Type I kerogen. Prior to pyrolysis, the kerogen was isolated from the sample (powdered to 0.175–1.150 mm) via demineralization with HF and HCl. The TOC content of the kerogen (unextracted) was 83.16%.

Pyrolysis was conducted with a confined system. The detailed procedure has been described previously (Behar et al., 1991; Pan et al., 2006; Wei et al., 2012; Jia et al., 2014). Au tube reactors were used with ca. 1 g aliquots of the kerogen. Each aliquot was loaded into 4 gold tubes (each with ca. 250 mg kerogen) and sealed under Ar. There were 16 stainless steel vessels, each with 4 tubes containing the kerogen samples. Each vessel was connected to a pressure waterline and placed in a single oven. A constant pressure of 50 MPa was maintained during pyrolysis. The pyrolysis temperature was programmed at 5 °C/h from room temperature to 300 °C in 10 h and subsequently to the final target temperature. With the aim of precisely evaluating the structural changes during the maturity range R_o 0.60–1.60%, the experiment was designed with 16 temperature points (Table 1). For each designated point, the corresponding maturity was calculated (Table 1) using the Easy $\%R_o$ model (Sweeney and Burnham, 1990).

After pyrolysis, the gas generated was collected in a special vacuum collector connected to an Agilent 6890N gas chromatography (GC) instrument modified by Wasson ECE Instrumentation for determination of gas composition. The Au tubes were pierced with a needle in a high vacuum chamber at room temperature, the gas flowing into the line. A specified amount of the collected gas was automatically transferred to the GC instrument for analysis (Pan et al., 2006; Jia et al., 2014).

For volatile hydrocarbon (C_6–C_{14}) recovery, another Au tube was rinsed and put into an 8 ml bottle with 4 ml *n*-pentane. The tube was pierced with a needle under the solution. After 20 min, the Au tube in the bottle was cut into two pieces quickly and returned to the bottle. Before quantitative analysis of the C_6–C_{14} compounds,

Table 1
Composition obtained from quantitative ^{13}C DP MAS NMR spectra.

Sample	Easy $\%R_o$	T (°C)[a]	220–190 ppm, %	190–165 ppm, %	Aromatic carbon (165–92 ppm, %)				Aliphatic carbon (92–0 ppm, %)						
			C=O	COO	ArCO	ArCC	ArC_{bridge}	ArCH	Alkyl C—O	C	CH	$(CH_2)_n$	CH_2(C2)	CH_{3aro}	CH_{3ali}
MM9[b]	0.43	non	0.1	2.6	4.5	8.4	8.1	9.7	0.0	4.8	3.2	51.0	2.5	2.8	2.5
M9K-1	0.60	324	1.2	2.5	4.1	11.1	9.2	7.8	1.1	3.1	3.7	46.8	3.4	3.4	2.1
M9K-2	0.70	344	0.1	1.6	3.8	13.7	12.3	9.1	1.7	3.2	4.4	39.9	4.0	3.5	2.7
M9K-3	0.80	364	0.0	1.7	4.4	16.4	14.8	9.5	1.7	2.9	5.5	36.4	1.9	2.5	2.9
M9K-5	0.90	379	2.2	4.9	6.5	20.1	19.8	13.7	0.2	2.6	3.3	10.0	4.6	3.0	2.3
M9K-6	0.95	385	0.6	1.6	4.0	17.5	25.4	22.8	1.4	2.4	4.9	9.4	3.6	2.5	3.9
M9K-7	1.00	390	0.1	1.2	4.0	18.3	28.0	24.8	0.5	1.6	4.4	8.5	2.8	2.7	3.3
M9K-8	1.05	396	0.0	0.7	2.8	16.1	29.1	29.8	0.4	1.5	4.2	7.1	1.9	3.3	3.1
M9K-9	1.10	400	0.2	1.4	3.8	17.1	29.4	28.3	0.2	0.8	3.3	7.2	1.7	3.2	3.4
M9K-10	1.15	405	0.0	1.4	3.9	18.2	31.2	28.5	0.2	0.7	2.2	5.6	1.9	2.7	3.4
M9K-11	1.20	409	0.3	1.3	3.4	18.5	31.7	29.6	0.5	0.0	1.8	4.9	1.5	2.9	3.7
M9K-12	1.25	414	0.5	1.5	3.2	16.2	31.5	34.4	0.1	0.0	1.3	3.2	1.5	2.7	3.8
M9K-13	1.30	418	0.0	1.1	2.9	15.5	31.4	35.8	0.1	0.0	1.1	3.7	1.5	2.6	4.3
M9K-14	1.40	426	0.1	1.3	3.4	16.3	32.2	35.9	0.2	0.0	1.1	1.9	1.3	2.7	3.7
M9K-15	1.50	434	0.6	1.2	3.3	16.3	32.8	36.8	0.2	0.0	1.1	1.0	1.2	2.3	3.2
M9K-16	1.60	441	0.7	1.3	3.2	16.2	33.0	37.7	0.0	0.0	1.2	1.0	0.7	2.1	3.0

[a] Pyrolysis temperature.
[b] Non-pyrolyzed Maoming oil shale kerogen.

an internal standard (n-$C_{24}D_{50}$) was added to the bottle. For the C_{14+} fraction analysis, Au tube opening was carried out at ambient temperature under atmospheric pressure. The cut off tubes with pyrolyzed kerogen were wrapped with extracted filter paper and extracted in a Soxhlet apparatus with dichloromethane:MeOH (93:7, v/v) for 72 h. After extraction, the solvent was evaporated and the extract weighed. The extract was deasphalted and separated using silica gel column chromatography into saturates (Sat), aromatics (Aro) and resins. The 4 fractions were dried and weighed. The insoluble residue was recovered from the filter paper, dried and weighed. Each residue was analyzed for elemental composition (C, H, O, N) and Rock-Eval parameters (S_2, HI).

The solid state ^{13}C-NMR spectra of the extracted kerogen residue were acquired with a Bruker DRX-400 on a 4 mm probe at 14,000 Hz carbon frequency with quantitative ^{13}C direct DP MAS. Cross polarization/spin-lattice relaxation time/total sideband suppression (CP T_1-TOSS) was used to measure recycle delays of $5T_1^C$ to ensure that all the carbon sites were ≥95% relaxed (Mao et al., 2000). The conjunction of DP MAS with CP T_1-TOSS is a viable approach for the quantitative NMR analysis of kerogen (Mao et al., 2000, 2010). To provide a visual image of the structural modification during artificial maturation, five kerogen molecular models representing different maturity were constructed according to the following sequence (Li et al., 2014; Ungerer et al., 2015):

(i) Gather together the elemental composition data and structural parameters from elemental analysis and ^{13}C DP MAS NMR; the parameters included f_a, X_{BP} and the atomic ratios H/C, O/C and N/C.
(ii) Select a total number of C atoms (N_C = 150–250) and determine the number of H atoms, N atoms and O atoms based on the corresponding atomic ratios from elemental analysis.
(iii) Obtain the number of aromatic carbons (N_{Ca}) by multiplying N_C by aromaticity (f_a).
(iv) Adopt the type and number of aromatic units in the kerogen to match the number of aromatic carbons and value of X_{BP}.
(v) Build an initial version of the model, matching elemental compositional data and NMR derived structural data.
(vi) Draw the structure of the kerogen model with Chemsketch software (ACD/labs, 2016) and apply gNMR 5.0.6 software (Ivorysoft) to compute the ^{13}C NMR spectra for the macromolecular structure.

The structure was subsequently modified according to trial and error procedure until a unit with optimal composition was obtained, whose calculated spectra matched best the experimental ^{13}C NMR spectra.

3. Results and discussion

3.1. Quantitative solid state ^{13}C DP MAS NMR

Quantitative ^{13}C DP MAS NMR spectra for the kerogen and the residue remaining after pyrolysis, arranged in order of increasing Easy %R_o, are shown in Fig. 1. The resonances were classified into 6 groups. Peaks at 62–0 ppm, 92–62 ppm, 150–92 ppm, 165–150 ppm, 190–165 ppm and 220–190 ppm are non-polar alkyls, O-alkyls, aromatics, aromatic C—O, COO and NC=O, and ketones, quinones and aldehydes, respectively (Trewhella et al., 1986; Patience et al., 1992; Lille et al., 2003; Kelemen et al., 2007; Mao et al., 2010). The fractions of various carbons for the kerogen and the kerogen residues are shown in Table 1.

3.1.1. Variation in aromaticity and aromatic groups

The aromatic region evolved from a minor proportion at R_o 0.43% to become the dominant feature in the NMR spectra corresponding to Easy %R_o above 0.90 (Fig. 1). The f_a values (Table 2) for the residue were obtained directly by integrating the 165–92 ppm region from the quantitative ^{13}C DP MAS spectra (Table 1).

The relationship between aromaticity and R_o (Fig. 2a) was positive but not linear, showing an obvious three stage behavior. In the first, from R_o 0.43% to Easy %R_o 0.80, f_a increased from 30.7% to 44.6%. Then, an abrupt change occurred between Easy %R_o 0.80 and 0.90, where f_a increased significantly from 44.6% to 68.9% (Fig. 2a). Third, from Easy %R_o 0.90 to 1.60, the rate of increase of f_a slowed with maturation. Aromaticity increased from 68.9% to 90.1% at this stage. It is noteworthy that the drastic change in structure took place within a very narrow maturity interval, between Easy %R_o 0.80 and 0.90. The possible cause of the abrupt change is discussed in following section, and is similar to the coalification jump in vitrinite or liptinite in coal (Teichmuller and Durand, 1983; Bustin and Guo, 1999; Li et al., 2016).

Signals with chemical shifts between 165–150 ppm and 150–92 ppm were assigned to the polar aromatic C—O fraction (f_a^P) and nonpolar aromatic carbons, respectively (Table 1). Spectral editing technology such as dipolar dephasing should be applied to determine f_a^B and f_a^H because the protonated aromatic carbons resonate with the bridgehead aromatic carbons (f_a^B) (Mao and Schmidt-Rohr, 2004; Wei et al., 2005; Mao et al., 2010). However, exact data on the fraction of bridgehead carbons (f_a^B) were not available since the spectral editing techniques were not performed. Furthermore, resonances from alkylated aromatic carbon may overlap with bridgehead ones. Previous studies assumed that carbons resonating around 108 ppm in ^{13}C NMR spectra are protonated aromatic carbons and that those resonating around 130 ppm are bridgehead carbons (Mann et al., 1991; Patience et al., 1992; Wei et al., 2005). However, Mao et al. (2010) found that a significant amount of protonated carbons was present around 130 ppm. Here, we simply assumed that the carbons between 92 and 125 ppm were protonated aromatic carbons, and those between 125 and 135 ppm were bridgehead ones. The results based on these assumptions are quite reasonable (see Section 3.4).

The region between 150 and 92 ppm was de-convoluted into protonated aromatic carbons (f_a^H; 125–92 ppm), aromatic bridgehead carbons (f_a^B; 135–125 ppm) and branched aromatic carbons (f_a^S, carbons connected to a carbon in either an aliphatic segment or a separate aromatic ring through a biaryl zero mass bridge; 150–135 ppm). The $f_a^H + f_a^B$ value, obtained by integrating the 135–92 ppm region, showed a positive correlation with maturity (Table 1). The fraction of branched aromatic carbon (f_a^S) was obtained by integrating the 150–135 ppm region. The value of f_a^S increased with maturity until Easy %R_o 0.90 and then remained constant (Table 1); Fig. 2b). The fraction of aromatic C—O carbons is discussed below.

3.1.2. Change in aliphatic carbon

Signals with chemical shifts of 92–0 ppm were assigned to alkyl groups (Table 1). Spectra across the ranges 92–62 ppm and 62–0 ppm were integrated to obtain quantitative data for O-alkyls and nonpolar alkyls, respectively. The latter were de-convoluted into quaternary carbons (Cq), CH, $(CH_2)_n$ (mid-chain or in ring), C2 (CH_2 connected to CH_3), Φ-CH_3 (connected to an aromatic ring) and R-CH_3 (at the end of an aliphatic chain) signals, assisted by curve fitting with the simulation software PEAKFIT (Peakfit v4.12; (Table 1); Fig. 3). Peak assignment was according to Trewhella et al. (1986) and Lille et al. (2003).

The fraction of aliphatic carbon (f_{al}) decreased (Table 2) from 66.7% to 7.9% from R_o 0.43% to Easy %R_o 1.60 during pyrolysis, as shown in Fig. 2a. More drastically, the fraction of aliphatic carbon (f_{al}) decreased from 53.8% at Easy %R_o 0.80 to 24.1% kerogen at Easy

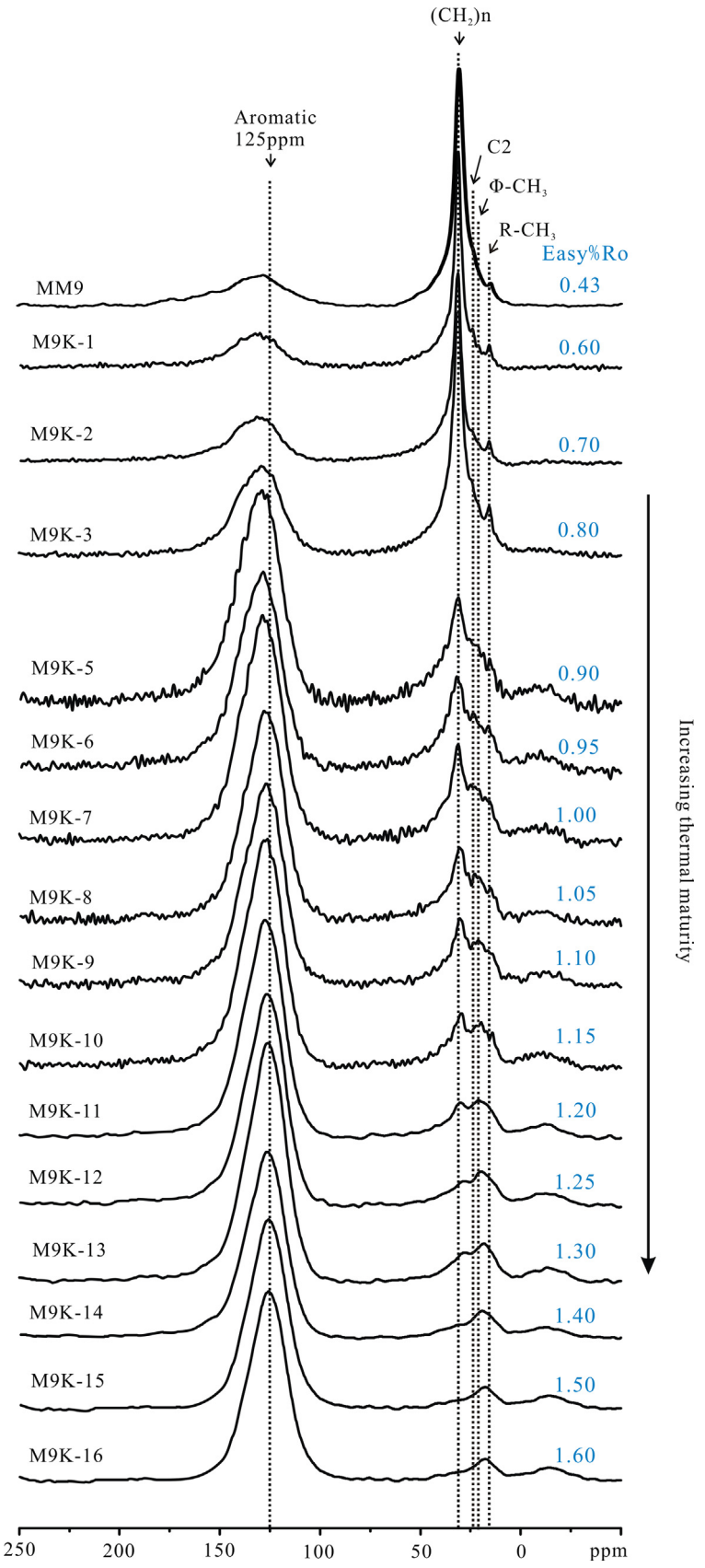

Fig. 1. Solid state ^{13}C DP MAS NMR spectra (maturity of kerogen residue increases from top to bottom).

Table 2
Carbon fractions and lattice parameters for kerogen residue.

Sample	Easy %R_o	T (°C)	f_a[a] (%)	f_{al}[b] (%)	f_{CH2}/f_{al}	f_{CH3}/f_{al}	f_{CH2}/f_{CH3}	Cn[c]	X_{BP}[d]
MM9	0.43	-	30.7	66.7	0.8	0.1	10.2	7.9	0.3569
M9K-1	0.60	324	32.7	63.6	0.8	0.1	9.1	5.7	0.4001
M9K-2	0.70	344	38.9	59.4	0.7	0.1	7.1	4.3	0.4643
M9K-3	0.80	364	44.6	53.8	0.7	0.1	7.0	3.4	0.4977
M9K-5	0.90	379	68.9	24.1	0.6	0.2	2.8	1.2	0.4788
M9K-6	0.95	385	69.7	28.2	0.5	0.2	2.0	1.6	0.5727
M9K-7	1.00	390	75.0	23.7	0.5	0.3	1.9	1.3	0.5946
M9K-8	1.05	396	77.8	21.5	0.4	0.3	1.4	1.3	0.5962
M9K-9	1.10	400	78.6	19.9	0.5	0.3	1.3	1.2	0.5964
M9K-10	1.15	405	81.8	16.8	0.5	0.4	1.2	0.9	0.6175
M9K-11	1.20	409	83.1	15.3	0.4	0.4	1.0	0.8	0.6168
M9K-12	1.25	414	85.4	12.6	0.4	0.5	0.7	0.8	0.5845
M9K-13	1.30	418	85.6	13.3	0.4	0.5	0.8	0.9	0.5798
M9K-14	1.40	426	87.7	10.9	0.3	0.6	0.5	0.7	0.5782
M9K-15	1.50	434	89.2	9.1	0.2	0.6	0.4	0.6	0.5829
M9K-16	1.60	441	90.1	7.9	0.2	0.6	0.3	0.5	0.5780

[a] Aromaticity.
[b] Fraction of aliphatic carbons.
[c] Aliphatic chain length.
[d] Ratio of aromatic bridgehead carbon to aromatic peripheral carbon.

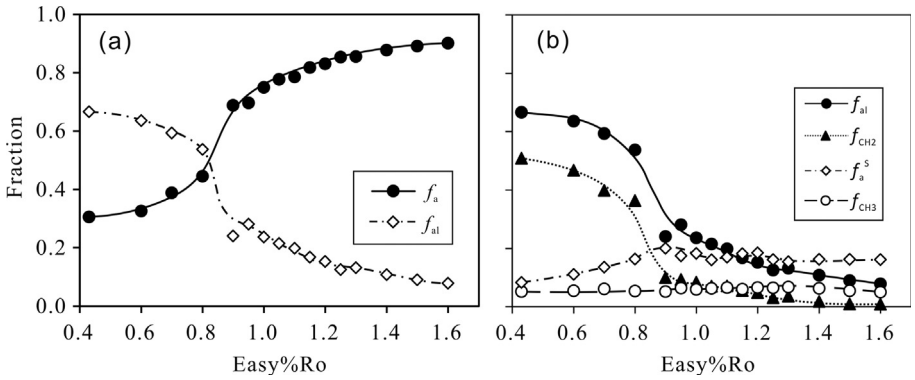

Fig. 2. Correlation between Easy %R_o and NMR structural parameters. (a) Fraction of aliphatic carbon (f_{al}) and aromaticity (f_a); (b) fraction of CH_3, $(CH_2)n$, aromatic C—C, and aliphatic carbon.

%R_o 0.90. After the sudden drop, the rate of f_{al} reduction decreased with maturity (Fig. 2a).

Spectra of lower maturity kerogen samples (R_o 0.43-Easy %R_o 0.80) had a remarkably sharp peak at ca. 31 ppm, corresponding to $(CH_2)_n$ groups (mid-chain or in ring; Fig. 1). The changing trend of $f_{(CH2)n}$ was very similar to that of f_{al} (Fig. 2b). Its fraction reduced significantly from 51.0% to 1.0% with maturity increasing from R_o 0.43% to Easy %R_o 1.60 (Table 1). A sharp reduction in $f_{(CH2)n}$ from Easy %R_o 0.80–0.90 was noteworthy (Fig. 2b). Actually, the value of f_{al} and f_{CH2} reduced by half between Easy %R_o 0.80 and 0.90 (Table 1); Fig. 2b). No such significant decrease was detected in other nonpolar aliphatic groups. The abrupt change in aliphatic carbons corresponded to the sudden growth in aromaticity.

For the CH_3 groups (methyl connected to aromatic rings and at the end of an aliphatic chain), we observed that it remained at a constant low fraction of 5.4–6.9% with respect to all carbons (Table 1; Fig. 2b). However, the aliphatic signal had a maximum peak near 20 ppm for kerogen residues with Easy %R_o > 1.20, indicating that the methyls became more prominent than CH_2 (Fig. 1.). Actually, f_{CH3}/f_{al} increased linearly from 0.1 to 0.6 with maturity increasing from R_o 0.43% to Easy %R_o 1.60, exceeding that of CH_2 [C2 and $(CH_2)_n$ in midchain or ring] groups after Easy %R_o 1.20 (i.e. after the oil window; Table 2; Fig. 4a). The relative enrichment of methyls in the alkyl groups during pyrolysis was also reported in studies of Type II kerogen and coal (Witte et al., 1988; Cao et al., 2013).

The greater intensity of CH and quaternary carbons reflected more branched points in the aliphatic chain. Our results confirm that the fraction of CH (f_{CH}) and that of the quaternary carbon group (f_{qC}) decreased with increasing maturity up to Easy %R_o 1.30 and remained at a constant low amount after that, suggesting that the branched chains were also thermally unstable and were cracked from the kerogen with increasing maturity. There were essentially no quaternary carbons after Easy %R_o 1.20 (Table 1).

3.1.3. Aliphatic chain length

The approximate average length of an aliphatic carbon chain (Cn′, half of a bridge or a side chain, including biaryl zero mass bridge) can be determined by dividing the fraction of aliphatic carbon (f_{al}) by the fraction of branched aromatic carbons (f_a^S; (Table 2); Kelemen et al., 2007; Fletcher et al., 2014; Clough et al., 2015). The correlation plot in Fig. 4b. shows an overall decrease in Cn' from ca. 8 at R_o 0.43% to <1 at Easy %R_o 1.60, consistent with the findings of Trewhella et al. (1986) and those of Fletcher et al. (2014) for the Green River Shale with equivalent maturity. The aliphatic chain length <1 above Easy %R_o 1.15 can be explained by the abundance of biaryl zero mass bridges at high maturity (Fletcher et al., 2014). We try to discuss a possible process mechanism in Section 3.4.

The f_{CH2}/f_{CH3} ratio (Table 2) is a common measure of aliphatic chemistry, since lower f_{CH2}/f_{CH3} values signify shorter aliphatic chains (Lin and Ritz, 1993). The relationship of f_{CH2}/f_{CH3} (Fig. 4b) with Easy %R_o here had two stages. In the first (R_o 0.43 – Easy %R_o 0.95), the ratio decreased rapidly from 10.2 to 2.0. Then, from Easy %R_o 0.95 to 1.60, the decrease was small from 2.0 to 0.3. Above Easy %R_o 1.20, the fraction of CH_3 groups exceeded that of CH_2

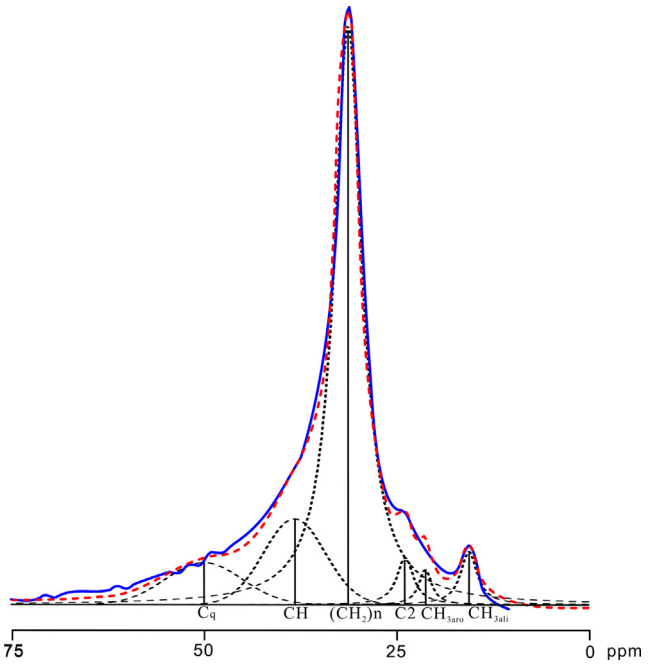

Fig. 3. Graph showing curve fitting for 62–0 ppm NMR region from kerogen residue M9K-2 sample. Peak assignment was according to previous studies (Trewhella et al., 1986; Patience et al., 1992; Lille et al., 2003; Kelemen et al., 2007; Mao et al., 2010). Solid envelopes represent measurements and dashed envelope a summary curve.

groups with respect to all the alkyl carbon groups (Table 2; Fig. 4a). These observations indicate that most of the long aliphatic chains was lost by a maturity of Easy %R_o 1.20.

3.1.4. O-containing functional groups

O-containing carbon species include alkyl C—O, aromatic C—O, carboxyl groups and carbonyl groups (ketones, aldehydes and quinones). The contents of these were directly obtained from quantitative ^{13}C DP MAS spectra by integrating the regions 92–62, 165–150, 190–165, and 220–190 ppm, respectively (Table 1). The content in residue M9K-5 of all of them was abnormally high (Table 1). This agreed with the increase in O/C of M9k-5 vs. M9K-3 (Fig. 5b). The total O-linked carbons accounted for only ca. 6% of all carbons. A slight, if any, decreasing trend of these groups existed with increasing maturity (Fig. 5a). The aromatic C—O groups were the most abundant of the O-containing carbons, followed by carboxyl groups (COO^-) and the alkyl C—O and carbonyl groups (Fig. 5a).

3.2. Results of elemental and Rock-Eval analysis

The results of elemental analysis and Rock-Eval pyrolysis of the extracted kerogen sample MM9 and residue from pyrolysis are shown in Table 3, Figs. 5b, 6 and 7. The C content of the residue at Easy %R_o 0.60 was higher than the extracted kerogen MM9. This may result from the loss of O. Then, the C content decreased continuously from 73.5% (at Easy %R_o 0.60) to a minimum of 45.3% (at Easy %R_o 0.90) and increased from the minimum to 64.9% (at Easy %R_o 1.60). Continuous H loss was observed throughout the experiment, with a marked decrease from 9.2% to 4.1% in the interval between R_o 0.43% and Easy %R_o 0.90 and a slower decrease after Easy %R_o 0.90 (Fig. 6). The O content of kerogen MM9 (R_o 0.43) was 13.7%. Sample M9K-1 with Easy %R_o 0.60 (at the beginning of catagenesis) had lost half of the O content vs. the initial kerogen sample. Then, the O content increased from 8.3% at Easy %R_o 0.80 to 15.72% at Easy %R_o 0.90 and decreased slightly to 12.4% at Easy %R_o 1.60. The N composition remained low and constant during pyrolysis (Fig. 6).

H/C decreased with maturity due to hydrocarbon generation (Table 3; Fig. 5b). Like the changing trend for O content, O/C (Fig. 5b) had an obvious increase between Easy %R_o 0.80 and 0.90 from 0.10 to 0.26. This was due to the preferential bulk elimination of hydrogen and carbon at this stage (Tissot and Welte, 1984). After the increase, O/C decreased to 0.14 at Easy %R_o 1.60 (Fig. 5b). These elemental analysis results were consistent with those of the NMR analysis discussed above. According to the NMR data, the fraction of O-containing carbon groups in the residue remained low and constant with maturation, with an abrupt increase at Easy %R_o 0.90 (Fig. 5a). This points to the same conclusion that, during the maturation interval Easy %R_o 0.60–1.60, no more O containing groups were cracked from the kerogen. Most O was removed as H_2O, CO and CO_2 before the mature stage (Tissot and Welte, 1984).

The S_2 value (Table 3) decreased with maturation from 602.0 mg/g at R_o 0.43% to 7.8 mg/g at Easy %R_o 1.60. The hydrogen index (HI) can be used to show the hydrocarbon potential of kerogen or rocks. It dropped from 799.0 mg/g TOC at R_o 0.43% to 12.1 mg/g TOC at Easy %R_o 1.60 (Table 3; Fig. 7a). It had a significant decrease in a narrow thermal window of Easy %R_o 0.80–0.90 and was <100 mg/g with maturity above Easy %R_o 1.00. More than half of the generation potential of the initial kerogen was released in the Easy %R_o interval 0.80–0.90 (Fig. 7a). This meant that the residual petroleum potential of the kerogen decreased with increasing maturity and that majority of the hydrocarbon potential of the Type I kerogen had been lost before Easy %R_o 0.90. The sudden drop in HI during Easy %R_o 0.80–0.90 was in good agreement with the abrupt change in aliphatic carbon mentioned above. The low hydrocarbon generation potential remaining above Easy %R_o 0.90 indicated by S_2 and HI corresponded to the low and constant

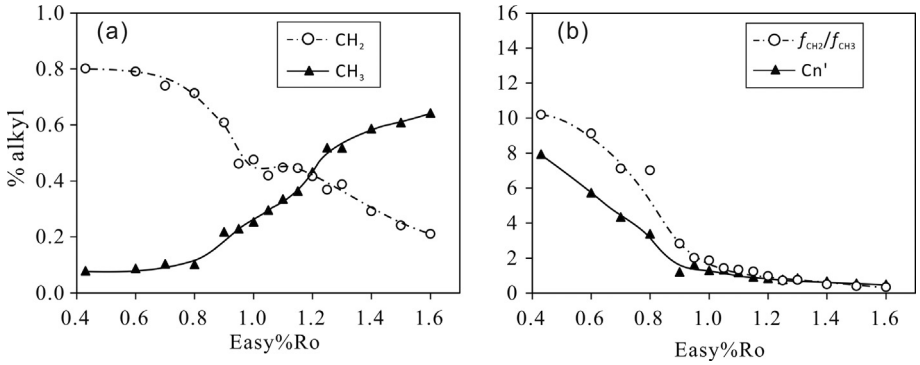

Fig. 4. Correlation between Easy %R_o and NMR lattice parameters. (a) Fraction of CH_3 and fraction of CH_2 in the alkyl components; (b) ratio of f_{CH2}/f_{CH3} and average aliphatic carbon chain length (Cn′).

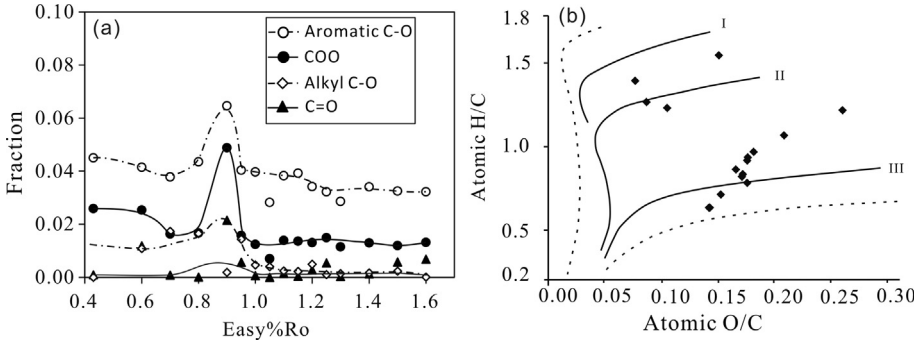

Fig. 5. (a) Variation in fractions of carbonyl (C=O), carboxyl (COO), aromatic C—O and alkyl C—O with Easy %R_o; (b) van Krevelen diagram of H/C vs. O/C for kerogen residue.

Table 3
Rock-Eval and elemental analysis of insoluble kerogen residue for NMR study.

Sample	Easy %R_o	T (°C)	Rock-Eval			Elemental analysis				H/Catomic	O/Catomic
			S_1[a] (mg/g)	S_2[a] (mg/g)	HI[b] (mg/g)	C (wt%)	H (wt%)	N (wt%)	O (wt%)		
MM9	0.43	-	2.1	602.0	799.0	71.0	9.2	1.2	13.7	1.56	0.15
M9K-1	0.60	324	0.8	530.0	721.3	73.5	8.5	1.8	7.4	1.39	0.08
M9K-2	0.70	344	1.1	427.2	596.4	71.6	7.6	2.1	8.2	1.27	0.09
M9K-3	0.80	364	1.1	328.9	549.0	59.9	6.1	1.9	8.3	1.23	0.10
M9K-5	0.90	379	0.9	58.1	128.1	45.3	4.1	2.0	15.7	1.07	0.26
M9K-6	0.95	385	1.1	67.2	130.8	51.4	4.6	2.6	14.3	1.06	0.21
M9K-7	1.00	390	0.9	61.3	105.6	58.0	4.7	2.8	14.0	0.96	0.18
M9K-8	1.05	396	0.7	49.0	83.1	59.0	4.6	2.7	13.9	0.93	0.18
M9K-9	1.10	400	0.8	47.0	78.5	59.9	4.6	2.9	14.0	0.91	0.18
M9K-10	1.15	405	0.7	35.1	56.9	61.8	4.4	3.1	13.6	0.86	0.17
M9K-11	1.20	409	0.4	25.5	41.5	61.4	4.0	2.9	14.4	0.78	0.18
M9K-12	1.25	414	0.6	17.0	27.2	62.5	4.3	3.0	14.2	0.82	0.17
M9K-13	1.30	418	0.3	20.2	32.3	62.5	4.3	3.0	14.3	0.83	0.17
M9K-14	1.40	426	0.5	12.0	18.9	63.3	3.7	2.8	12.8	0.71	0.15
M9K-15	1.50	434	0.4	8.0	12.3	65.2	3.4	2.7	12.4	0.63	0.14
M9K-16	1.60	441	0.4	7.8	12.1	64.9	3.4	2.7	12.4	0.63	0.14

[a] In mg HC/g kerogen (HC, hydrocarbon).
[b] In mg HC/g TOC.

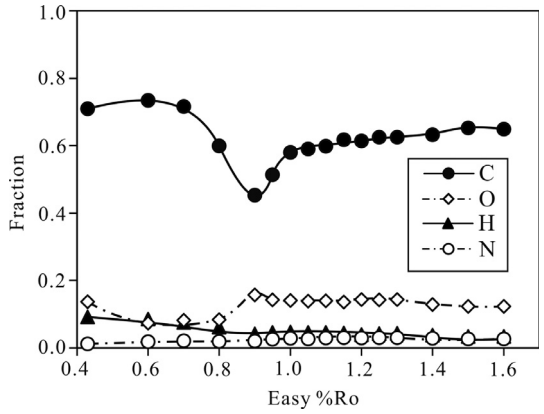

Fig. 6. Diagram showing elemental weight composition of kerogen residue with Easy %R_o.

value of f_{al} after Easy %R_o 0.90, indicating that there was only a small number of aliphatic groups in the residue, representing elimination of the oil potential from the kerogen residue (Fig. 7a). This indicates that chemical structural evolution controls the hydrocarbon generation potential.

3.3. Pyrolysis product characteristics

Yields of organic products (kerogen residue, $C_{14+NSOs}$, C_{14+Aro}, C_{14+Sat}) are shown in Table 4. The yields are normalized to 100% and shown in Fig. 8.

The yield of insoluble kerogen residue started with a linear downward trend extending to a minimum of 77.2 mg/g TOC at Easy %R_o 0.95, suggesting that >90% of the OM was thermally decomposed (Table 4). The amount of residue increased after the minimum at R_o 0.95% to 438.2 mg/g TOC at Easy %R_o 1.60, suggesting that most of the insoluble solid residue originated from secondary cracking reactions (Behar et al., 2010).

The C_{14+} fraction reached peak generation at Easy %R_o 0.95 and then started to crack with increasing maturity (Table 4, Fig. 8). The yield of NSOs (resin and asphaltene), similar to that of C_{14+}, reached a maximum of 589.2 mg/g TOC at Easy %R_o 0.95. Then, a progressive decrease in yield of NSOs was observed (Table 4, Fig. 8).

As shown in Fig. 9., the NSOs were generated as soon as the pyrolysis began, accounting for 93.16% of the whole C_{14+} yield at Easy %R_o 0.60. The proportion of NSOs relative to C_{14+} yield decreased gradually as maturity increased, accounting for 28.20% at Easy %R_o 1.40; it then increased to 38.34% at Easy %R_o 1.60 (Fig. 9). The yield of C_{14+} aromatics was similar to that of C_{14+} saturates before Easy %R_o 1.00 (Fig. 9). Then, the yield of C_{14+} aromatics stopped growing and decreased continuously from 107.9 mg/g TOC at Easy %R_o 1.10 to 54.3 mg/g TOC at Easy %R_o 1.60. The yield of C_{14+} saturates continued to increase until Easy %R_o 1.25, where a maximum of 177.4 mg HC/g TOC was obtained. The yield of C_{14+} saturates was reduced after Easy %R_o 1.25, corresponding to $f_{CH2}/f_{CH3} < 1$ after Easy %R_o 1.20, suggesting the end of oil window.

The yield of total hydrocarbon gases (C_{1-5}) and light hydrocarbons (C_{6-14}) increased continuously with maturity between Easy %R_o 0.60 and 1.60 (Table 4; Fig. 8). The maximum yield of the C_{14+} fraction occurred at Easy %R_o 0.80–0.90 (Table 4; Fig. 8). The

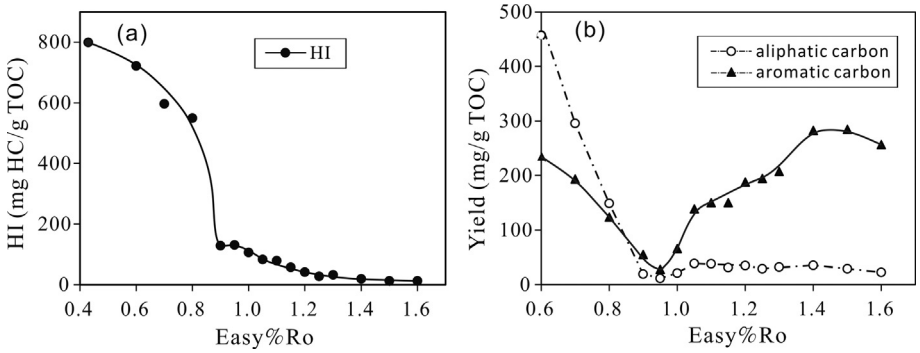

Fig. 7. (a) Rock-Eval hydrogen index (HI); (b) yield of aliphatic carbon and aromatic carbon in solid residue.

Table 4
Hydrocarbon composition from Au tube pyrolysis.

Sample	Easy %R_o	T (°C)	C_{1-5} mg/g TOC	C_{6-14} mg/g TOC	$C_{14+\ Sat}$ mg/g TOC	$C_{14+\ Aro}$ mg/g TOC	$C_{14+\ NSOs}$ mg/g TOC	Residual kerogen yield mg/g TOC	Aliphatic carbon yield mg/g TOC	Aromatic carbon yield mg/g TOC
M9K-1	0.60	324	2.2	13.6	9.4	8.1	160.4	976.5	456.5	234.4
M9K-2	0.70	344	4.6	20.6	20.0	35.8	327.4	693.7	295.1	193.4
M9K-3	0.80	364	10.2	29.9	43.6	59.7	456.7	462.0	148.8	123.4
M9K-5	0.90	379	20.0	52.5	86.6	87.7	576.7	176.3	19.3	55.0
M9K-6	0.95	385	24.2	53.0	105.0	98.5	589.2	77.2	11.2	27.6
M9K-7	1.00	390	31.7	65.3	110.7	101.4	535.9	151.1	20.8	65.8
M9K-8	1.05	396	32.6	71.9	130.9	102.2	364.1	302.5	38.4	138.8
M9K-9	1.10	400	39.4	81.5	138.7	107.9	329.9	319.3	38.0	150.2
M9K-10	1.15	405	43.9	90.9	151.3	102.1	334.1	297.1	30.8	150.1
M9K-11	1.20	409	50.3	102.2	162.7	97.4	248.8	368.0	34.6	187.7
M9K-12	1.25	414	63.3	115.3	177.4	109.8	202.0	363.4	28.6	193.9
M9K-13	1.30	418	64.3	126.8	173.9	95.3	181.3	387.5	32.1	207.2
M9K-14	1.40	426	80.2	152.9	148.0	67.9	97.0	508.6	35.0	282.4
M9K-15	1.50	434	94.9	173.8	137.1	68.3	98.2	488.7	28.9	284.2
M9K-16	1.60	441	117.7	218.4	101.1	54.3	114.8	438.2	22.4	256.3

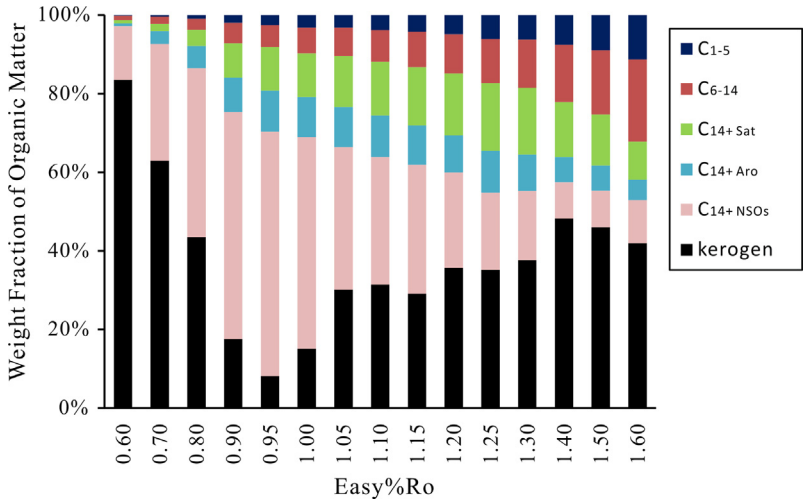

Fig. 8. Diagram illustrating changes in yield of kerogen residue, NSOs (asphaltene + resin), C_{14+}Sat, C_{14+}Aro, C_{6-14}, and gas from kerogen pyrolysis, normalized to 100%.

maximum saturated hydrocarbon generation correlated approximately to Easy %R_o 1.15–1.25 (Table 4).

3.4. Kerogen structure models accounting for maturity

The ratio of the aromatic bridge carbon to aromatic carbon along the edges of the aromatic rings, $X_{BP} = f_a^B/(f_a^H + f_a^P + f_a^S)$, is closely linked to the size of the condensed aromatic clusters. Based on the available experimental conditions, the exact fraction of bridgehead carbon cannot be obtained, since there is heavy spectral overlap between protonated aromatic carbons and bridgehead carbons and between bridgehead carbons and alkylated aromatic carbons in highly condensed systems (Mao et al., 2010). Here, we simply assumed that carbons that resonate between 92 and 125 ppm were protonated aromatic carbons and that carbons that resonate between 125 and 135 ppm were bridgehead carbons. Values of

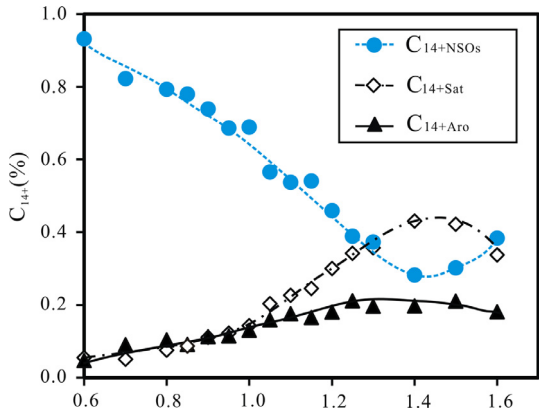

Fig. 9. Fractions of saturated hydrocarbons, aromatic hydrocarbons and NSOs with respect to C_{14+} yield with increasing maturity.

X_{BP} for the kerogen residue calculated from the NMR data are shown in Table 2.

The five kerogen molecular models built correspond to (A) the immature stage, (B) before the abrupt structural change, (C) after the structural abrupt change, (D) before the end of the oil window, with Easy %R_o 1.10 and (E) at the end of the oil window.

3.4.1. Immature kerogen model

The model for the initial kerogen sample, at the immature stage with R_o 0.43%, is indicated in Fig. 10. Previous studies indicated that aromatic units of oil asphaltene molecules are dominated by 4–8 aromatic rings despite the oil maturity (Mullins, 2010). Moreover, asphaltenes are a product of the cracking of kerogen during thermal degradation. Based on the above consideration, we adopted 1–5 ring aromatic units as the structural skeleton for the non-pyrolyzed kerogen (Table 5). We also included one polycyclic saturated structure, as a sterane backbone, to represent as much information as possible. Other parts, such as the aliphatic structures or O containing functional groups, were attached to the aromatic units on the basis of the structural parameter constants. A comparison between the computed ^{13}C NMR data for the kerogen model and the experimental spectrum is shown in Fig. 10.

The composition of the initial kerogen model is $C_{248}H_{365}N_3O_{20}$. With R_o 0.43%, the model is very rich in long aliphatic chains (avg. 10; Fig. 10). The existence of monocyclic, di-aromatics and tri-aromatic units in the initial kerogen corresponds to the ability of the Maoming oil shale kerogen to generate soluble aromatic hydrocarbons during evolution.

3.4.2. Matured kerogen model

The kerogen model M9K-3, with Easy %R_o 0.80, is shown in Fig. 11. It has a formula of $C_{204}H_{269}N_3O_{12}$. The calculated ^{13}C NMR spectrum for this model is in good agreement with the experimental ^{13}C NMR spectrum (Fig. 11). Five polyaromatic units are included, composed of 2–6 aromatic rings (Table 5). The number of aromatic carbons and aliphatic carbons is 90 and 111, respectively. The other 4 carbons are attached with carboxyl or carbonyl groups. The aliphatic chain length in model M9K-3 is shorter than that of the initial kerogen model, mainly between 4 and 8 carbons in a chain, in good agreement with the structural parameters determined from the NMR spectra. The structural modification of model M9K-3 compared with the initial kerogen model reflects the idea that, during maturation, oil and gas are generated through the breaking of C—C bonds or the breaking of other unstable functional groups such as ester groups or ether bridges. Part of the petroleum generation potential of the initial kerogen is released during maturation from R_o 0.43% to Easy %R_o 0.80, while more than half of the potential still remains. The increase in X_{BP} of M9K-3 compared with MM9 initial kerogen can result from the release of small ring units, and not necessarily because of the aromatization of aliphatic carbons.

3.4.3. Kerogen model close to peak oil window

Model M9K-5 (Easy %R_o 0.90) was obtained with a composition of $C_{140}H_{122}N_4O_{13}$ and is shown in Fig. 12. A comparison between the computed ^{13}C NMR spectrum for the kerogen model and the experimental spectrum is shown in Fig. 12. The model has 6

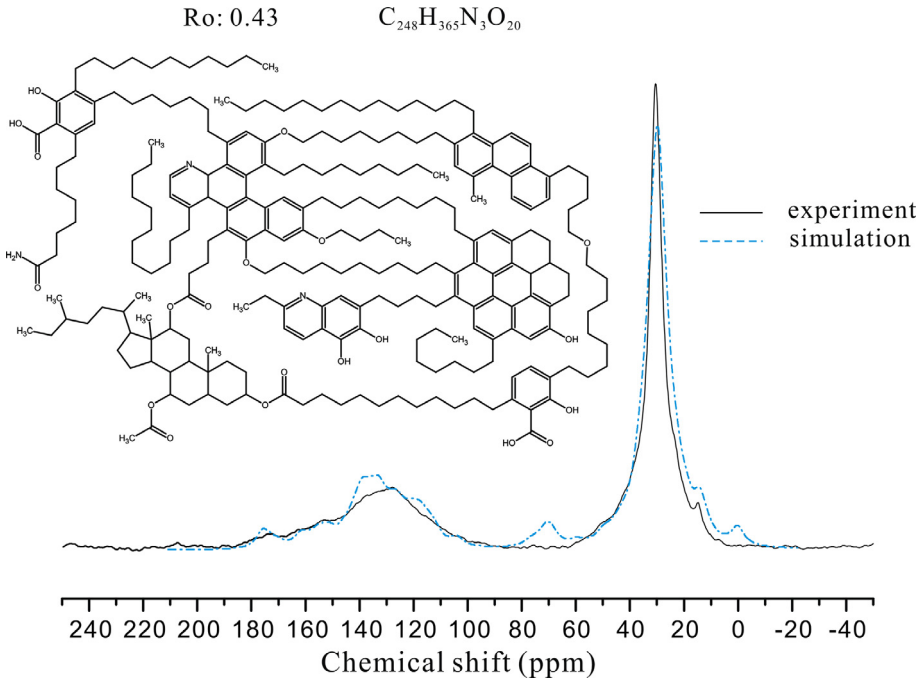

Fig. 10. Macromolecular structure model of MM9 kerogen and comparison with ^{13}C NMR spectra.

Table 5
Structural parameters for kerogen models.

Sample	Easy %R_o (R_o)	f_a (%)	X_{BP}	Number of aromatic structure units							Avg. size of polyaromatic domains[b]
				1 Ring	2 Ring	3 Ring	4 Ring	5 Ring	6 Ring	7 Ring	
MM9	0.43[a]	29.84	0.3571	2	1	1	1	1			2.7
M9K-3	0.8	42.65	0.5000		1	1	1	1	1		4.0
M9K-5	0.9	68.57	0.4706		2	1	1	1	1		3.7
M9K-9	1.1	77.88	0.5962				2	2	1	2	5.4

[a] R_o.
[b] Number of rings.

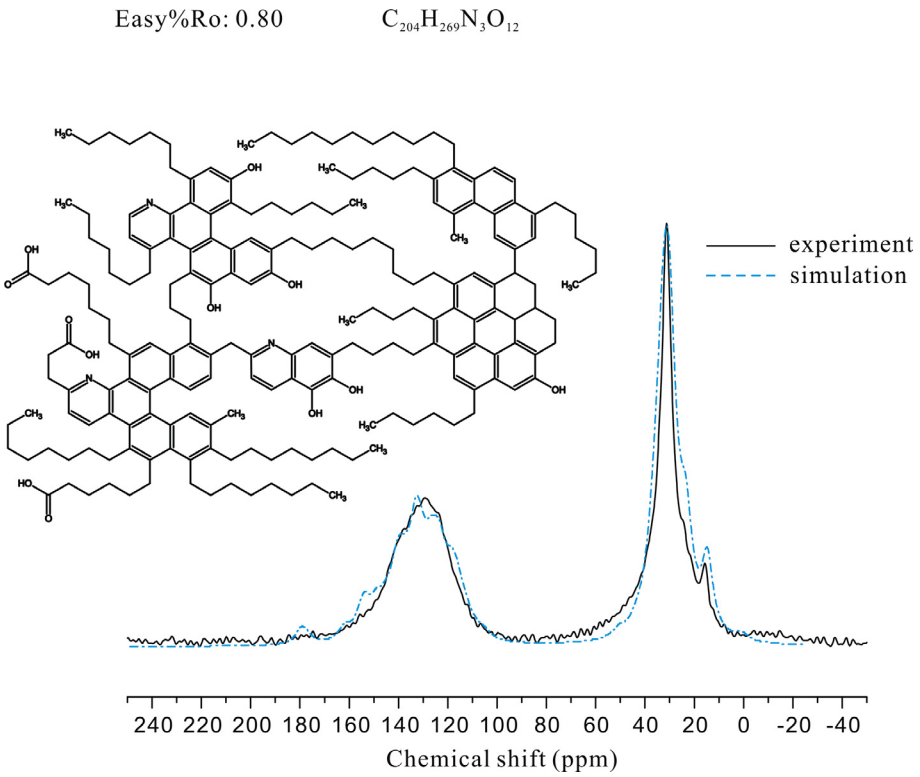

Fig. 11. Matured kerogen structure (M9K-3) and comparison with ^{13}C NMR spectra.

polyaromatic units with much shorter aliphatic chains attached than model M9K-3 (Table 5). We obtained fair agreement with the fraction of aromatic carbons and value of X_{BP} (Table 5). Most of the long aliphatic chains are ruptured or cracked out of the kerogen residue. The high potential for generating paraffinic oil or gas no longer exists. The main part of the carbon content is in the polyaromatic units instead of the aliphatic chains such as the model of M9K-3 or the initial kerogen. It is noteworthy that the value of X_{BP} of sample M9K-5 is essentially the same as that of sample M9K-3. This indicates that the average cluster size of the aromatic units did not increase during this stage.

3.4.4. Kerogen model at late oil window

The model for M9K-9 is shown in Fig. 13. A comparison between the computed ^{13}C NMR spectrum of the kerogen model and experimental spectrum is shown in Fig. 13. The composition is $C_{208}H_{168}N_4O_{10}$. The values of f_a and X_{BP} in the model are in good agreement with the experimental analysis (Table 2; Table 5). The model is composed of larger (4–7 rings) polyaromatic units. After the peak in the oil window and before the end of the window, the M9K-9 kerogen model has an even shorter aliphatic chain length than M9K-5. There is barely any potential for generating paraffinic oil from M9K-9 residue. The low aliphatic content remaining in the residue may contribute to the generation of hydrocarbon gas at higher maturity. The value of X_{BP} is 0.5964, higher than that of M9K-5. Small aromatic units no longer exist at this stage.

3.4.5. Kerogen model at end of oil window

The kerogen model of the M9K-13 residue is shown in Fig. 14. The formula is $C_{212}H_{151}N_3O_{10}$. A comparison between the computed ^{13}C NMR of the kerogen model and experimental spectrum is shown in Fig. 14. The aromaticity (84.43%) is in good agreement with ^{13}C DP MAS NMR data (85.6%; Table 2; Table 5). Eight polyaromatic units are included, composed of 4–7 rings (Table 5). This model allows a good match of X_{BP} with the NMR data. The aliphatic bonds are mainly methyls attached directly to aromatic rings or biaryl zero mass bonds connecting two aromatic carbons. If this is the case, then it is reasonable that the fraction of alkylated aromatics is higher than that of the alkyl carbons obtained with the NMR data (Table 2).

Note that the X_{BP} does not increase along with maturation from Easy %R_o 1.10 to 1.30, whereas the aromaticity increases from 78.6% to 85.6%. During this maturation stage, the shortening of

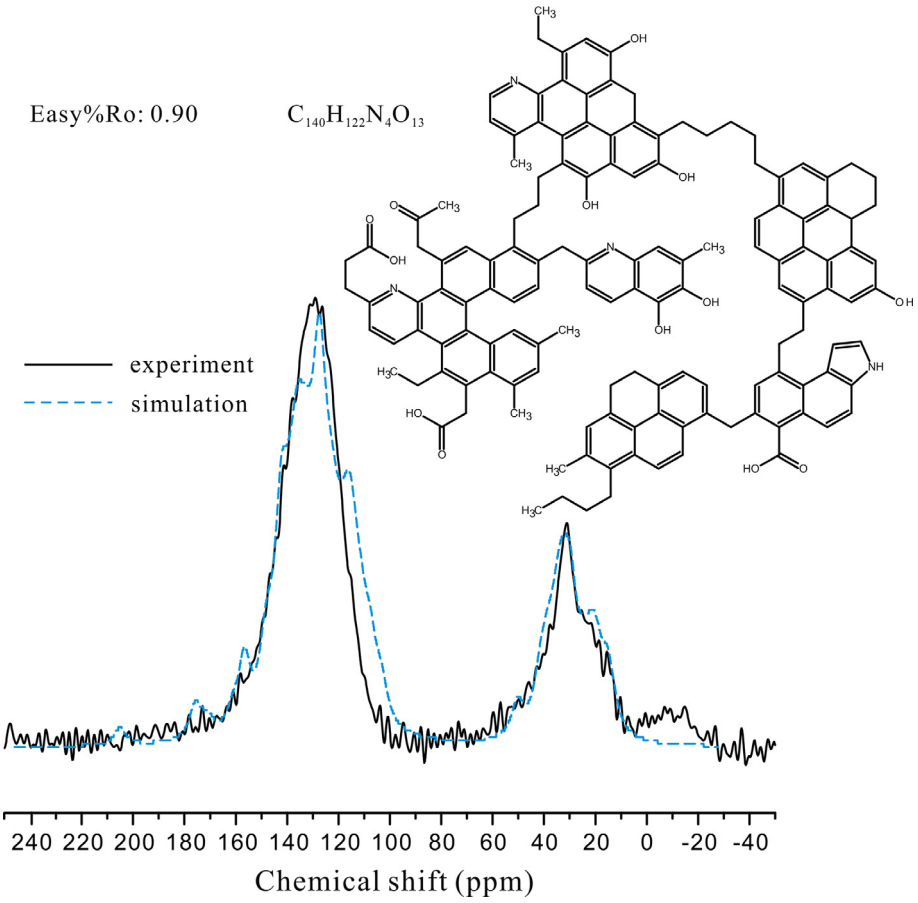

Fig. 12. Structure of kerogen (M9K-5, Easy %R_o 0.90) and ^{13}C NMR spectra.

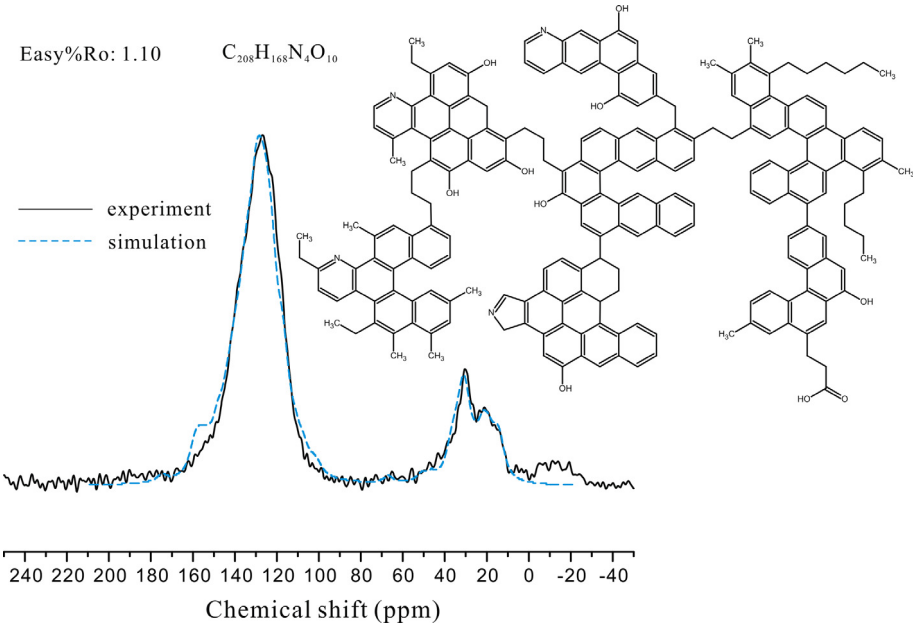

Fig. 13. Kerogen model showing structure after peak oil and ^{13}C NMR spectra.

the aliphatic segments has almost finished. The increase in aromaticity is primarily due to the growth of the aromatic units. However, there is no increase in the average cluster size, as shown by the value of X_{BP} or the structure models drawn (Table 2; Table 5). Therefore, we propose that the growth in aromaticity is due to the increase in the aromatic cluster numbers. The clusters are

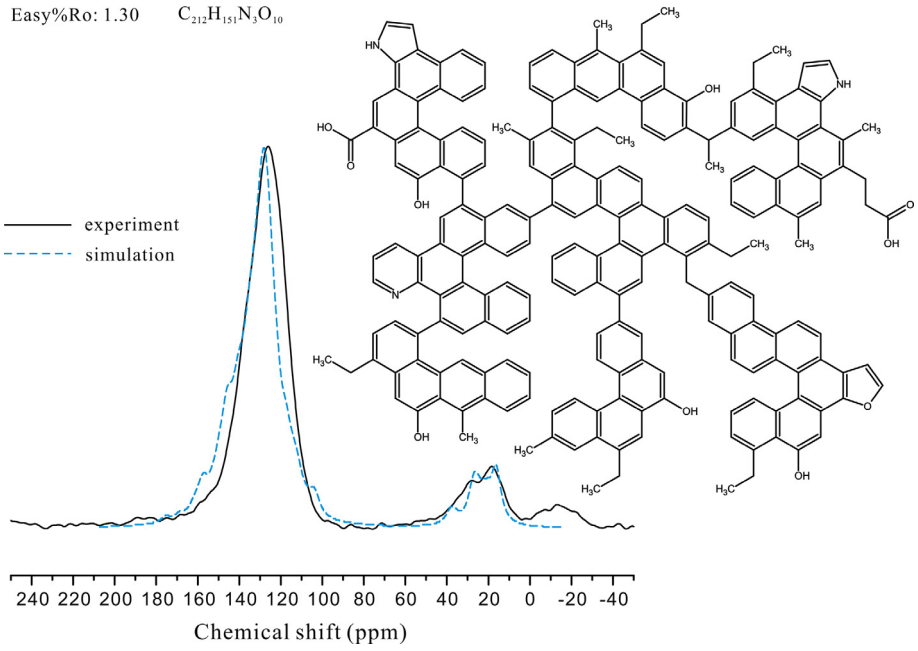

Fig. 14. Kerogen structure model and ^{13}C NMR spectra at the end of the oil window.

connected with each other through very short aliphatic segments or even through biaryl zero mass bridges, as shown in model M9K-13 (Fig. 14). Then, it is reasonable to conclude that the newly added aromatic clusters in the kerogen residue come from the asphaltenes, cracked from the kerogen at a lower maturity stage. This conclusion is consistent with the characteristics of hydrocarbon generation discussed in Section 3.3.

Moreover, the existence of biaryl zero mass bridges and very short aliphatic segments between two aromatic clusters in the kerogen structure generates a high degree of reticulation, which could be the nanopores that can provide storage space for the hydrocarbon gas.

3.5. Structure jump

Abrupt changes or jumps occurred in the NMR characteristics of the residue at ca. Easy $\%R_o$ 0.80–0.90 and 1.15–1.25. These abrupt changes are similar to the coalification jump in vitrinite or liptinite in coals (Teichmuller and Durand, 1983; Bustin and Guo, 1999; Li et al., 2016).

The jump at peak oil window (Easy $\%R_o$ 0.80–0.90) is reflected in (i) an abrupt increase in f_a (Fig. 2a), (ii) a marked decrease in f_{al} and f_{CH2} (Fig. 2b), (iii) a deceleration of the decrease in f_{CH2}/f_{al} (Fig. 4a), (iv) a turning point around Easy $\%R_o$ 0.90 in the relationship line for Cn′-Easy $\%R_o$ and f_{CH2}/f_{CH3}-Easy $\%R_o$ (Fig. 4b), (v) an elevation in the fraction of O containing groups and O/C at Easy $\%R_o$ 0.90 (Fig. 5), (vi) a major loss of hydrocarbon generation potential during Easy $\%R_o$ 0.80–0.90 (Fig. 7a) and (vii) the peak in C_{14+} yield at Easy $\%R_o$ 0.95 (Fig. 8). Taken together, the jump at peak oil window highlights a marked reduction in the fraction of aliphatic $(CH_2)_n$. The concurrence of major loss of hydrocarbon generation potential and reaching maximum production of C_{14+} with the sudden reduction of aliphatic (CH_2)i at this point confirming that the essence of generation of petroleum from kerogen is the shortening of kerogen aliphatic chains.

The jump at the end of the oil window (Easy $\%R_o$ 1.20–1.30%) is characterized by (i) $f_{CH2}/f_{CH3} < 1$, i.e. higher intensity of methyls than of CH_2 groups in the NMR spectra (Fig. 1), (ii) Cn′ (aliphatic chain length) < 1 (Fig. 4) and (iii) the crossover of the C_{14+Sat} fraction with the $C_{14+NSOs}$ fraction with respect to the yield of C_{14+} at Easy $\%R_o$ 1.30 (Fig. 9). After the jump, there are very few long aliphatic chains (>2) left in the residue, the jump corresponding roughly to the second coalification jump (Teichmuller and Durand, 1983).

3.6. Development of aromaticity during maturation

While aromaticity increases with maturity for all types of kerogen, the actual relationship differs (Dennis et al., 1982; Russell et al., 1983; Takeda and Asakawa, 1988; Witte et al., 1988; Carr and Williamson, 1990; Patience et al., 1992; Wei et al., 2005; Werner-Zwanziger et al., 2005; Mao et al., 2010; Fletcher et al., 2014). Nevertheless, in the previous studies, there was no reported mechanism for the evolution of aromaticity of Type I kerogen. Quantitative NMR analysis in combination with geochemical analysis of kerogen residue and hydrocarbon generation from pyrolysis in a closed system allowed us to probe the mechanism.

By multiplying the residual kerogen yield (mg/g TOC), elemental carbon content, and the carbon fraction in the NMR analysis, the absolute yield (mg/g TOC) of aromatic carbons and aliphatic carbons could be acquired (Table 4, Fig. 7b). The yield curve for aromatic carbon clearly shows that, with increasing maturity, the aromatic carbon yield decreased at first and reached a minimum at R_o 0.95%. Then, an increase in aromatic carbon yield was observed. A constant pronounced number of aliphatic carbons and a relatively smaller number of aromatic carbons were lost as soon as pyrolysis began and extended to Easy $\%R_o$ 0.95. During this period, the yield of kerogen residue decreased (Fig. 8). The yield of aliphatic carbons remained low and constant above Easy $\%R_o$ 0.95. However, the yield of aromatic carbons increased after Easy $\%R_o$ 0.95.

These observations suggest that, below Easy $\%R_o$ 0.95, both aromatic structures and aliphatic chains were cracked from the kerogen, but with relatively more cleavage of aliphatic bonds (Fig. 7b). The decrease in aromatic carbon yield may be due to elimination of small aromatic rings, either through liberation of aromatic hydrocarbons or of bitumen (Rouxhet and Robin, 1978). No aromatic rings were formed in this stage. At the Easy $\%R_o$ 0.80–0.90 interval, both aliphatic and aromatic carbon yield still decreased. However, during this stage, the yield of aromatic carbons exceeded that of the aliphatic carbons, accompanied by a relative enrichment in the aromatic groups (Fig. 7b). Therefore, the steep slope in the rela-

tionship between f_a and Easy %R_o at an Easy %R_o range of 0.80–0.90 resulted from the relatively more extensive cleavage of aliphatic bonds. Above Easy %R_o 0.95 (after peak oil generation), the absolute yield of aromatic carbon increased with maturity, indicating that new aromatic structures were added to the aromatic units. Above Easy %R_o 0.90, the aliphatic carbon yield stayed constant and low. Therefore, the increase in f_a at the third stage above Easy %R_o 0.95 was mainly due to the formation of new aromatic structures from condensation or the aromatization of bitumen. This explanation agrees well with the conclusions in Section 3.4.

3.7. Contribution from different carbon types to hydrocarbon generation potential

The majority of the hydrocarbon potential for the Type I kerogen was lost before Easy %R_o 0.90, as indicated from S_2 and HI and shown in the kerogen model series proposed. According to the residue yield during pyrolysis, >90% of the initial kerogen was thermally decomposed at Easy %R_o 0.95. Corresponding to this, the total amount of pyrolysis product (C_{1-5} + C_{6-14} + C_{14+} fraction) reached peak yield at Easy %R_o 0.95 (Fig. 8). These observations indicate that the peak in oil generation during pyrolysis occurred around Easy %R_o 0.95. The reducing fraction of C_{14+} NSOs means that the NSOs were the predominant compounds generated during kerogen cracking at low maturity, and were subsequently cracked to oil, gas and insoluble residue with maturity, consistent with previous studies (Tissot and Welte, 1984; Behar et al., 2010).

The absolute weight of both aliphatic and aromatic carbons in the kerogen residue decreased below Easy %R_o 0.95, with the aliphatic carbons decreasing more drastically. Therefore, the kerogen cracking led to cleavage of aliphatic bonds and aromatic structures simultaneously. Both contributed to the oil and gas generation before Easy %R_o 0.95. Here, the aromatic hydrocarbons generated from the Maoming kerogen reached a maximum at ca. Easy %R_o 1.10. Then, a decrease occurred (Table 4). Behar et al. (2010) attribute the decrease in the yield of C_{14+} aromatics to secondary cracking. The decrease in formation of C_{14+} aromatics from the cracking of kerogen or NSOs can also be a reasonable explanation. However, interestingly, despite the up and down behavior during pyrolysis, the yield of aromatic carbons in the residue at Easy %R_o 1.60 returned to the residue yield at Easy %R_o 0.60 (Table 4).

The decrease in f_{al} was caused mainly by the cleavage of $(CH_2)_n$ segments from the kerogen, as indicated by the parallelism between the changing curve of f_{al} and $f_{(CH2)n}$ (Fig. 2b). Moreover, CH_3 groups contributed little to hydrocarbon generation between R_o 0.43 and Easy %R_o 1.60, since f_{CH3} remained low and constant during pyrolysis. In the over-mature stage, CH_3 contributed to the CH_4 production reported in studies of coal kerogen (Cao et al., 2013). Therefore, we conclude that the CH_3 groups have a high bond dissociation energy and can only be released at the high maturity stage to contribute to gas generation.

4. Conclusions

Pyrolysis of Maoming oil shale kerogen, which is Type I, was performed with a closed Au tube system under 50 MPa constant pressure. The targeted maturity interval was Easy %R_o 0.60–1.60 to simulate shale oil formation. The yield of generated gas, light hydrocarbons, the C_{14+} fraction and the insoluble residue were quantitatively measured. The combination of quantitative solid state ^{13}C DP MAS NMR analysis with artificial maturation provided new insights into the structural changes and hydrocarbon generation mechanism for Type I kerogen with increasing maturity.

The aromaticity (f_a) of the kerogen residue from pyrolysis increased from 30.7 to 90.1%. The relationship showed a positive non-linear three stage correlation between f_a and maturity (R_o, %), which is obviously different from that of Type II or Type III kerogen. Both aromatic and aliphatic carbons were cracked from the kerogen structure before Easy %R_o 0.95. The bulk selective removal of aliphatic carbons was responsible for the f_a increase. The steep slope between Easy %R_o 0.80 and 0.90 in the f_a-Easy %R_o relationship resulted from relatively more cleavage of the aliphatic carbons and then the aromatic carbons exceeding the aliphatic ones after Easy %R_o 0.80, which corresponded to peak oil generation. At the third stage, Easy %R_o 0.95–1.60, the f_a-Easy %R_o relationship was curved. The f_a increased gently due to the formation of new aromatic clusters from the aromatization of bitumen. This new formation of aromatic structures in pyrobitumen was responsible for the residue yield increase after Easy %R_o 0.95.

Abrupt changes or jumps in the structure of kerogen residue were observed at ca. Easy %R_o 0.80–0.90 and 1.15–1.25, corresponding to the peak oil window and the end of the oil window, respectively.

Five kerogen structure models with different evolution stages within the oil window were constructed on the basis of elemental composition and structural parameters derived from ^{13}C DP MAS NMR spectra. The series of structures provided a visual image of structure modification during maturation. Both the kerogen models and the NMR data suggest that the average aromatic cluster size increased gently before the peak in the oil window, and then stayed almost constant until the end of the oil window (Table 5). Our data indicate that the increasing nucleus size of the kerogen before the peak in the oil window was primarily due to degradation of small aromatic units. The increasing aromaticity after the peak oil window did not result from the increase in the average size of the aromatic units but was caused by new aromatic units being added to the kerogen structure from the bitumen by very short aliphatic chains or biaryl zero mass bridge bonds.

Aliphatic chains contributed most of the hydrocarbon potential during Easy %R_o 0.60–1.60. Nevertheless, hydrocarbons may also be formed from the release of small aromatic rings. The cleavage of aliphatic $(CH_2)_n$ bonds was the main cause of a decrease in the aliphatic fraction and was the main source of potential hydrocarbon generation before Easy %R_o 1.20. Meanwhile, the CH_3 groups remained at a constant low fraction of all the carbons, contributing little to hydrocarbon generation in the maturity interval studied. A high dissociation bond energy prevented the release of CH_3 functional groups in the oil window.

Acknowledgments

The authors are grateful to two anonymous reviewers for constructive comments and suggestions. We would like to thank Prof. H. Lu for providing the oil shale sample. We are grateful to Prof. J. Liu and Dr. X. Zhang for pyrolysis experiment assistance and ^{13}C NMR analysis. We thank Dr. W. Li for guidance on the molecular model construction method from NMR. The study was supported by the Foundation for Innovative Research Groups of the National Natural Science Foundation of China (Grant No. 41621062), the National Basic Research Program of China (Grant No. 2014CB239100) and the NSFC of China (Grant Nos. 41273059; 41072096).

Associate Editor—**C.C. Walters**

References

ACD/Labs, 2016. <http://www.acdlabs.com/resources/freeware/chemsketch/>.
Behar, F., Vandenbroucke, M., 1987. Chemical modeling of kerogens. Organic Geochemistry 11, 15–24.

Behar, F., Kressmann, S., Rudkiewicz, J.L., Vandenbroucke, M., 1991. Experimental simulation in a confined system and kinetic modeling of kerogen and oil cracking. Organic Geochemistry 19, 173–189.
Behar, F., Roy, S., Jarvie, D., 2010. Artificial maturation of a Type I kerogen in closed system: mass balance and kinetic modelling. Organic Geochemistry 41, 1235–1247.
Bustin, R.M., Guo, Y., 1999. Abrupt changes (jumps) in reflectance values and chemical compositions of artificial charcoals and inertinite in coals. International Journal of Coal Geology 38, 237–260.
Cao, X., Chappell, M.A., Schimmelmann, A., Mastalerz, M., Li, Y., Hu, W., Mao, J., 2013. Chemical structure changes in kerogen from bituminous coal in response to dike intrusions as investigated by advanced solid-state ^{13}C NMR spectroscopy. International Journal of Coal Geology 108, 53–64.
Carr, A.D., Williamson, J.E., 1990. The relationship between aromaticity, vitrinite reflectance and maceral composition of coals: implications for the use of vitrinite reflectance as a maturation parameter. Organic Geochemistry 16, 313–323.
Clough, A., Sigle, J.L., Jacobi, D., Sheremata, J., White, J.L., 2015. Characterization of kerogen and source rock maturation using solid-state NMR spectroscopy. Energy & Fuels 29, 6370–6382.
Dennis, L.W., Maciel, G.E., Hatcher, P.G., Simoneit, B.R.T., 1982. ^{13}C nuclear magnetic resonance studies of kerogen from Cretaceous black shales thermally altered by basaltic intrusions and laboratory simulations. Geochimica et Cosmochimica Acta 46, 901–907.
Durand-Souron, C., 1980. Thermogravimetric analysis and associated techniques applied to kerogens. In: Durand, B. (Ed.), Kerogen, Insoluble Organic Matter from Sedimentary Rocks. Editions Technip, Paris, pp. 143–161.
Fletcher, T.H., Gills, R., Adams, J., Hall, T., 2014. Characterization of macromolecular structure elements from a Green River oil shale, II. Characterization of pyrolysis products by ^{13}C NMR, GC/MS, and FTIR. Energy & Fuels 28, 2959–2970.
gNMR, Version 5.0.6-DEMO by Cherwell Scientific Publishing. <http://www.cherwell.com>.
Jia, W., Wang, Q., Liu, J., Peng, P., Li, B., Lu, J., 2014. The effect of oil expulsion or retention on further thermal degradation of kerogen at the high maturity stage: a pyrolysis study of type II kerogen from Pingliang shale, China. Organic Geochemistry 71, 17–29.
Kelemen, S.R., Afeworki, M., Gorbaty, M.I., Sansone, M., Kwiatek, P.J., Walters, C.C., Freund, H., Siskin, M., 2007. Direct characterization of kerogen by X-ray and solid-state ^{13}C nuclear magnetic resonance methods. Energy & Fuels 21, 1548–1561.
Li, W., Zhu, Y., Song, Y., Wang, M., 2014. Study of a vitrinite macromolecular structure evolution control mechanism of the energy barrier in hydrocarbon generation. Energy & Fuels 28, 500–509.
Li, W., Zhu, Y.-M., Wang, G., Jiang, B., 2016. Characterization of coalification jumps during high rank coal chemical structure evolution. Fuel 185, 298–304.
Lille, Ü., Heinmaa, I., Pehk, T., 2003. Molecular model of Estonian kukersite kerogen evaluated by ^{13}C MAS NMR spectra. Fuel 82, 799–804.
Lin, R., Ritz, G.P., 1993. Studying individual macerals using i.r. microspectroscopy, and implications on oil versus gas/condensate proneness and "low-rank" generation. Organic Geochemistry 20, 695–706.
Mann, A.L., Patience, R.L., Poplett, I.J.F., 1991. Determination of molecular structure of kerogens using ^{13}C NMR spectroscopy: I. The effects of variation in kerogen type. Geochimica et Cosmochimica Acta 55, 2259–2268.
Mao, J.D., Hu, W.-G., Schmidt-Rohr, K., Davies, G., Ghabbour, E.A., Xing, B., 2000. Quantitative characterization of humic substances by solid-state $^{13}C^{13}C$ nuclear magnetic resonance. Soil Science Society of America Journal 64, 873–884.
Mao, J.D., Schmidt-Rohr, K., 2004. Accurate quantification of aromaticity and nonprotonated aromatic carbon fraction in natural organic matter by ^{13}C solid-state nuclear magnetic resonance. Environmental Science and Technology 38, 2680–2684.
Mao, J., Fang, X., Lan, Y., Schimmelmann, A., Mastalerz, M., Xu, L., Schmidt-Rohr, K., 2010. Chemical and nanometer-scale structure of kerogen and its change during thermal maturation investigated by advanced solid-state ^{13}C NMR spectroscopy. Geochimica et Cosmochimica Acta 74, 2110–2127.
Mullins, O.C., 2010. The modified Yen Model. Energy & Fuels 24, 2179–2207.
Pan, C., Yu, L., Liu, J., Fu, J., 2006. Chemical and carbon isotopic fractionations of gaseous hydrocarbons during abiogenic oxidation. Earth and Planetary Science Letters 246, 70–89.
Patience, R.L., Mann, A.L., Poplett, I.J.F., 1992. Determination of molecular structure of kerogen using ^{13}C NMR spectroscopy: II. The effects of thermal maturation on kerogens from marine sediments. Geochimica et Cosmochimica Acta 56, 2725–2742.
Peakfit, Version v4.12–DEMO by Systat Software Inc. <http://www.systatsoftware.com>.
Qian, J., Yin, L., 2008. Oil Shale: Petroleum Alternative. China Petrochemical Press, Beijing, pp. 14–23.
Qin, K., Chen, D., Li, Z., 1991. A new method to estimate the oil and gas potential of coals and kerogens by solid state ^{13}C NMR spectroscopy. Organic Geochemistry 17, 865–872.
Rouxhet, P.G., Robin, P.L., 1978. Infrared study of the evolution of kerogens of different origins during catagenesis and pyrolysis. Fuel 57, 533–540.
Russell, N.J.Wilson, M.A., Pugmire, R.J., Grant, D.M., 1983. Preliminary studies on the aromaticity of Australian coals-solid state NMR techniques. Fuel 62, 601–605.
Siskin, M., Scouten, C.G., Rose, K.D., Aczel, T., Colgrove, S.G., Pabst, R.E., 1995. Detailed structural characterization of the organic material in Rundle Ramsay Crossing and Green River oil shales. In: Snape, C. (Ed.), Composition, Geochemistry and Conversion of Oil Shales. Springer, Netherlands, Dordrecht, pp. 143–158.
Sweeney, J.J., Burnham, A.K., 1990. Evaluation of a simple model of vitrinite reflectance based on chemical kinetics (1). American Association of Petroleum Geologists Bulletin 74, 1559–1570.
Takeda, N., Asakawa, T., 1988. Study of petroleum generation by pyrolysis—I. Pyrolysis experiments by Rock-Eval and assumption of molecular structural change of kerogen using ^{13}C-NMR. Applied Geochemistry 3, 441–453.
Teichmuller, M., Durand, B., 1983. Fluorescence microscopical rank studies on liptinites and vitrinites in peat and coals, and comparison with results of the rock-eval pyrolysis. International Journal of Coal Geology 2, 197–230.
Tissot, B.P., Welte, D.H., 1984. Petroleum Formation and Occurrence. Springer Verlag, Berlin.
Tong, J., Jiang, X., Han, X., Wang, X., 2016. Evaluation of the macromolecular structure of Huadian oil shale kerogen using molecular modeling. Fuel 181, 330–339.
Trewhella, M.J., Poplett, I.J., Grint, A., 1986. Structure of Green River oil shale kerogen: determination using solid state ^{13}C NMR spectroscopy. Fuel 65, 541–546.
Ungerer, P., Collell, J., Yiannourakou, M., 2015. Molecular modeling of the volumetric and thermodynamic properties of kerogen: influence of organic type and maturity. Energy & Fuels 29, 91–105.
Vandenbroucke, M., 1980. Structure of kerogens as seen by investigations on soluble extracts. In: Durand, B. (Ed.), Kerogen, Insoluble Organic Matter from Sedimentary Rocks. Editions Technip, Paris, pp. 415–443.
Vandenbroucke, M., 2003. Kerogen: from types to models of chemical structure. Oil & Gas Science and Technology 58, 243–269.
Vandenbroucke, M., Largeau, C., 2007. Kerogen origin, evolution and structure. Organic Geochemistry 38, 719–833.
Wei, Z., Gao, X., Zhang, D., Da, J., 2005. Assessment of thermal evolution of kerogen geopolymers with their structural parameters measured by solid-state ^{13}C NMR spectroscopy. Energy & Fuels 19, 240–250.
Wei, Z., Zou, Y.-R., Cai, Y., Wang, L., Luo, X., Peng, Pa., 2012. Kinetics of oil group-type generation and expulsion: an integrated application to Dongying Depression, Bohai Bay Basin, China. Organic Geochemistry 52, 1–12.
Werner-Zwanziger, U., Lis, G., Mastalerz, M., Schimmelmann, A., 2005. Thermal maturity of type II kerogen from the New Albany Shale assessed by ^{13}C CP/MAS NMR. Solid State Nuclear Magnetic Resonance 27, 140–148.
Witte, E.G., Schenk, H.J., Müller, P.J., Schwochau, K., 1988. Structural modifications of kerogen during natural evolution as derived from ^{13}C CP/MAS NMR, IR spectroscopy and Rock-Eval pyrolysis of Toarcian shales. Organic Geochemistry 13, 1039–1044.
Yen, T.F., 1976. Structural aspects of organic components in oil shales. In: Yen, T.F., George, V.C. (Eds.), Developments in Petroleum Science. Elsevier, Oxford, pp. 129–148.